Type of paper: Article

Title: Debris flow overflowing flexible barrier: physical process and drag load characteristics

Authors: Lingping Wang[1,2], Dongri Song[1,2]*, Gordon G. D. Zhou[1,2], Xiao Qing Chen[2], Min Xu[3,4], Clarence E. Choi[5], Peng Peng[6]

*Corresponding author: Dongri Song (drsong@imde.ac.cn)

1. School of River and Ocean Engineering, Chongqing Jiaotong University, Chongqing, China
2. Institute of Mountain Hazards and Environment, Chinese Academy of Sciences (CAS), Chengdu, China
3. School of Environment, Chengdu University of Technology, Chengdu, China
4. Geobrugg Chengdu Co., Ltd., Chengdu, China
5. Department of Civil Engineering, University of Hong Kong, Hong Kong SAR, China
6. PowerChina HuaDong Engineering Corporation Limited, Hangzhou, China

Debris flow overflowing flexible barrier: physical process and drag load characteristics

Abstract: The multiple-barrier mitigation strategy in the debris-flow source area is an effective approach to inhibit debris-flow entrainment and scale amplification along the flow path. However, less is known as debris flow overflows a filled barrier and cascades downstream.

The present study investigates the physical processes and load characteristics of debris-flow overflowing a model flexible barrier, using a well-instrumented medium-scale flume. Volumetric solid concentration is varied ranging from 0.4 to 0.6 so that the control factors (*e.g.,* state of liquefaction and turbulent drag) in the overflow process can be identified. The results demonstrate that effective stress is not observed in the incoming debris flows for solid concentration up to 0.6, denoting a contribution of turbulent drag to the overflow drag. The formed hydraulic jump substantially elevates the overflow depth above the flexible barrier, which has not been considered in the current design guideline. Decomposition of the total overflow load reveals that the increase in total load is actually dominated by the static load due to the elevated flow depth, rather than the turbulent drag. Downward momentum transfer to the lower section of barrier is observed and re-liquefaction of the deposited debris is a prerequisite for the downward momentum transfer. Different from the high solid-concentration cases, the deposit of low solid concentration (0.4) behind the barrier is partially drained with nontrivial effective stress, which further hinders the downwards momentum transfer to the base of barrier. The findings of present study indicate that the debris-flow properties are the key control factors for the complicated debris-barrier

interaction.

Keywords: debris flow; overflow; load model; flexible barrier; liquefaction

1. Introduction

The entrainment of debris flow along flow path substantially amplifies its scale (Iverson et al. 2011; Iverson and Ouyang 2015; Ouyang et al. 2015; Liu et al. 2021) and therefore the resulted destructive power to the downstream human lives and infrastructure (Chen et al. 2021a; Zhang et al. 2021). Current design principle of debris-flow mitigation structures is dedicated to building deposition barriers around the apex of debris-flow fan. Alternatively, barriers could also be installed upstream to the source area to inhibit the scale amplification along the flow path (Kwan et al. 2015; Vicari et al. 2021). The steel-net flexible barrier has become advantageous under this design principle, owing to its light weight, easy installation, high permeability to slurry phase, and aesthetic appearance in the hilly mountains (Wendeler et al. 2007; Wendeler 2016; Tan et al. 2020). Due to the steep gradient and narrow channel width in the upper catchment, cascade barriers are needed to intercept the debris volume and regulate the kinetic energy (Wendeler et al. 2008; Song et al. 2019b; Berger et al. 2021). Fig. 1 shows an example of multiple debris-flow flexible barriers upstream a railway in the west of Beijing. Among the processes of impact, filling, overflow, and landing under successive debris-flow surges (Ng et al. 2019; 2021; Speerli et al. 2010), overflow is less studied and its physical process (interaction with barrier and with the retained debris) remains unclear. Footages at the Illgraben site showing debris-flow filling and overflow processes is available at https://www.youtube.com/watch?v=4NIfCV4SVC0 and https://www.youtube.com/watch?v=0PsVhIQUUro. Some description of the overflow loading characteristics of Illgraben debris flows can be found in Wendeler (2016).

Current design guidelines (e.g., Kwan 2012; Wendeler et al. 2019) assume that the drag load localizes around the interface between the overflowing layer and static deposit, leading to the drag load concentrating on the crest of barrier (Fig. 2a). The field observation of Illgraben debris flow by McArdell et al. (2007) can be regarded as a special case of overflow. With a horizontal force plate at the crest of a check dam, the normal and shear stresses as well as pore fluid pressure were continuously measured. The ratio between shear stress and effective normal stress yields a Coulomb basal friction angle of 26° at the flow front, denoting the dominance of frictional component in the drag load.

The experimental investigation on the overflow issues cannot clearly distinguish the horizontal overflow (with barrier fully filled) from debris spill-out (Wong and Lam 2018). For the debris spill-out, the flow trajectory is approximately parallel to the barrier surface. Since the majority of debris-flow momentum flux has been resisted by the barrier, this loading scenario should be regarded as direct impact, rather than overflow. For the horizontal overflow, the flow trajectory is parallel to the incoming flow, denoting substantial momentum flux has been drained downstream. However, the proportion of momentum resisted by the barrier remains unknown. Moreover, the transient impact-filling-overflow process makes the dynamic response of barrier during loading rather complicated (Tan et al. 2020; Kong et al. 2021; Zhang and Huang 2021). The temporal and spatial variation of flow parameters (density, velocity, and depth) renders unreliable correlation with the dynamic response of barrier.

Based on rigorous conservation of momentum, a multi-parameter oveflow load model for dry dense granular flows has been proposed by Faug et al. (2009; 2012). To close the proposed model (i.e., the number of equations has to match that of parameters), constitutive

83 equation, geometrical relationship, and assumptions have to be adopted. The prerequisite is
84 that the physical processes and constitutive behavior are both well understood for dry granular
85 flows. For two-phase debris flows, the physical processes and constitutive behavior are still
86 unclear and serve as the key focus of this experimental study.

87 By using a medium-scale flume setup and a flexible barrier model, Song et al. (2022)
88 investigated the dynamic impact response of flexible barrier under three surge loads. Current
89 multiple-surge load model (e.g., Kwan 2012; Wendeler et al. 2019) was assessed through
90 measured load profile and state of static deposit. However, strong interaction (remixing)
91 between the flowing phase and deposited phase as well as downward momentum transfer
92 were revealed, which is the key limitation of current load model. This finding is also
93 instructive to the overflow process, which is not covered in Song et al. (2022) due to the
94 limited volume of prepared debris.

95 As a continuation of Song et al. (2022), this study increases the debris volume and
96 number of surges to investigate the physical process of overflow and the characteristics of
97 drag load. The existing debris-flow overflow load model is first briefly reviewed. Based on
98 the experimental results, the composition of overflow induced load and the control factors of
99 remixing process are revealed. Finally, the prospect of a rigorous overflow load model with
100 consideration of mass and momentum conservation is discussed.

101 2. Load model of debris-flow overflow

102 Natural debris flow is characterized by its multiple-surge behavior. A debris-resisting
103 barrier would experience the first impact, subsequent impact, and finally overflow (Fig. 2a) as
104 the barrier is completely filled up. Multiple-surge load model with allowance for surcharge

loading has been developed (Kwan 2012; Wendeler et al. 2019) based on rigorous conservation of momentum. For the first impact, the impact load F is the combination of both dynamic and static forces of the flowing layer with depth h (Song et al. 2021):

$$F = \alpha\rho v^2 hw + \frac{1}{2}k\rho g h^2 w \quad (1)$$

where α is the hydrodynamic pressure coefficient, ρ is bulk density of debris flow (kg/m^3), v and h are frontal velocity (m/s) and depth (m) of the incoming flow, w is width of barrier (m), k is the hydrostatic pressure coefficient, and g is gravitational acceleration of (m/s^2). The hydrodynamic pressure coefficient α is related to the flow regime (*i.e.*, Froude number, Hübl et al. 2009), inclusion of boulders (Scheidl et al. 2013), and structure form (Wang et al. 2018; Chen et al. 2021b). Moreover, α value is strongly affected by the stiffness of mitigation structures. The large deformation of flexible barrier could effectively elongate the duration of impact, resulting in a much lower α value (Song et al. 2019a). Currently, the recommended α value by the Geotechnical Engineering Office of Hong Kong is 1.5 for rigid mitigation structures (GEO 2020).For subsequent debris-flow impact, the impact load is a combination of both loads of the flowing layer and static deposit:

$$F = \alpha\rho v^2 hw + \frac{1}{2}k\rho g H^2 w \quad (2)$$

where H is the total height of both the static deposit and flowing layer.

Previous study has confirmed the reliability of the multiple-surge load model in predicting the total impact load. However, in terms of load distribution along barrier height, there is substantial discrepancy between the experimental measurement and model prediction. Specifically, the impact load concentrates on the lower section of barrier which should be

127 covered by the deposited debris, rather than the position of flowing layer. Analysis of the state
128 of static deposit reveals that the remixing process (interaction between the flowing layer and
129 deposited layer) is the cause of the re-liquefaction of deposited debris and downward
130 momentum transfer to the lower part of barrier (Song et al. 2022). This downward momentum
131 transfer indicates that the prediction of multiple-surge load model may not be conservative for
132 engineering design.

133 As for the drag load exerted by the overflowing debris, since the outflow velocity cannot
134 be predicted beforehand, the momentum flux intercepted by the barrier is unknown. The total
135 force (including drag load) is estimated based on the frictional and turbulent flow resistance
136 of the two-phase debris flow as well as the overall static load (Fig. 2a):

137 $$F = \rho g h(tan\varphi + \frac{v^2}{h\xi})wL + \frac{1}{2}k\rho g H^2 w \quad (3)$$

138 where φ is apparent friction angle (°), ξ is turbulent coefficient (m/s^2) based on the Voellmy
139 rheological model (Voellmy 1955), and L is the length of active wedge behind the barrier
140 (Kwan 2012).

141 3. Methodology: modeling debris-flow overflow in a medium-scale flume

142 The same model setup with Song et al. (2022) is adopted to study debris flow overtopping a
143 model flexible barrier. The instrumentation and test program are revised accordingly to serve
144 the targets of this study.

145 *3.1 Model setup*

146 The medium-scale concrete flume consists of a gate at the upstream, a linear
147 transportation zone, and a model flexible barrier at the downstream (Fig. 3a). The distance

148 from gate to model barrier is 7.15 m and the width between two sidewalls is 0.7 m (Fig. 3c).
149 The inclination of flume is constant at 12°. This relatively low inclination enhances the basal
150 flow resistance and limits the maximum solid concentration of debris flow to 0.6. The section
151 upstream of the gate is used as a container to store debris materials. Upon uplift of the gate,
152 the debris can be released to model a dam-break failure.

153 *3.2 Model flexible barrier*

154 Due to the nonlinear elasto-plastic loading behavior, it remains a difficulty to scale down
155 the properties of a prototype flexible barrier into the model scale (Ng et al. 2016). To reveal
156 the key interaction between debris flow and flexible barrier, a simplified model flexible
157 barrier is used. The 0.45 m high and 0.7 m wide model barrier consists of a net and four steel
158 strand cables which are isometrically installed on the net with a spacing of 0.15 m (Fig. 3c).
159 The model barrier is installed adjacent to basal sensing module 2 (Fig. 3a). The net is made of
160 high-density polyethylene is characterized with 5 mm net opening. Considering the typical
161 cable spacing in a prototype barrier is around 1.5 m (thus with a scale factor 1.5/0.15=10 for
162 the model barrier), 5 mm is equivalent to a net opening of 50 mm, which is typical for a
163 flexible barrier with a finer secondary mesh (Berger et al. 2021). When debris flow impacts
164 the model barrier, the debris first impinges the net surface, then the net transfers the impact
165 load to cables. Slack is provided in the net to ensure the debris impact load can be fully borne
166 by the horizontal cables.

167 In this barrier setup, flexibility provided by the energy dissipating devices and
168 deformable net is replaced by a 0.2 m prescribed deformation in the horizontal cable, *i.e.*, the
169 length of each horizontal cable is preset as 0.9 m. Both sides of the cables are fixed to the

concrete side walls using expansion bolts (for modeling of anchor foundation in prototype).

3.3 Instrumentation

The normal/shear stresses and pore fluid pressure are measured by two basal sensing modules (Fig. 3b) which are installed with their surface flush with the bed of flume (Fig. 3a). Basal sensing module consists of a triaxial load cell for measurement of basal normal stress and shear stress (measured forces divided by the sensing area), and a Pore Pressure Transducer (PPT) for measurement of pore fluid pressure. The open end of PPT is covered by a 0.4 mm steel mesh, which could effectively filter the coarse particles and transmit the pressure of fluid phase. Prior to each test, PPT has to be manually saturated to ensure the accuracy of pore fluid pressure measurement. The measurement of basal load might be affected by the size effect of basal sensing module. There are two considerations for designing the size of force plate. 1. The force plate should be as large as possible to smooth-out the impact load of single particles; 2. The force plate should be as small as possible to enhance the resolution of measurement in the flow direction. The diameter of force plate is 120 mm (Fig. 3b).

The flow depth of debris flow is measured by both ultrasonic and laser sensors, which are installed directly above the two basal sensing modules. One more pair is installed in-between to accurately derive the flow velocity and depth prior to overflow (Fig. 3a and Fig. 6). The ultrasonic sensor located in front of the gate serves as a trigger to determine the moment of debris-flow release. Video cameras are installed upstream, downstream, and over the model flexible barrier (Fig. 3a) to record the impact, filling, and overflow processes. Miniature tension load cells are connected on the four cables of model barrier to record the

192 tensile force induced by debris impact and overflow (Fig. 3c). A multiple-channel NI data
193 acquisition system is adopted to synchronously record the measured data.

194 *3.4 Debris flow material*

195 Granular material from the debris-flow deposits in the Jiangjia Gully, near the
196 Dongchuan Debris Flow Observation and Research Station (DDFORS), is used in this study.
197 The coarse particles in the deposits are removed by using a 20 mm × 20 mm steel sieve. The
198 particle size distribution of the material, with median particle size 2.84 mm, is shown in Fig. 4.
199 After sieving, the relative proportion is clay:silt:sand:gravel = 2.0:6.5:32.7:58.8.

200 Removal of coarse particles increases the percentage of fine particles (clay and silt) and
201 this would result in a higher pore fluid pressure and low flow resistance (low effective stress)
202 in the modelled debris flows (Kaitna et al. 2016). These fine particles, combined with water,
203 form a solid-liquid unsorted slurry, which is of great significance to the movement of debris
204 flow (Fei et al. 1991). In this study, as suggested by Cui et al. (2005), the maximum particle
205 size of the debris-flow slurry is 1.2 mm. Given the fine material below 1.2 mm is considered
206 as part of liquid phase, the new median particle size is 4.30 mm (Fig. 4).

207 *3.5 Test program and procedure*

208 To investigate the impact and overflow of debris flows with distinct flow characteristics,
209 the volumetric solid concentration (including the fine particles with particle size smaller than
210 1.2 mm) is set to 0.4, 0.5, and 0.6, ranging from a dilute to dense flow regime. The
211 corresponding bulk densities are 1660, 1825, and 1990 kg/m^3, respectively. Based on the
212 rheological tests of debris-flow slurry in Jiangjia Gully (Yang et al. 2013), the viscosities are

213 determined as 0.19, 0.41, and 0.88 Pa·s, respectively. Each experimental series is designed
214 with four independent releases, and the interval between two releases is about 30 min but also
215 controlled by the weather condition of the day. The volume of a single release is 0.2 m^3 (0.15
216 m^3 in Song et al. 2022). Details of the test program are summarized in Table 1. The first three
217 surges (0.6 m^3) completely fill up the barrier, and the 4th surge would form the overflow. Due
218 to the concrete flume bed, this study does not consider the entrainment of completely
219 consolidated materials of antecedent debris flow events; while the entrainment of loose
220 deposits of the previous surges has to be considered.

221 Once the model is prepared, the configured debris-flow mixture is loaded behind the gate
222 and is manually stirred to ensure the solid-liquid mixture remain well mixed. The
223 impact/overflow processes last about two seconds (Fig. 5, 7, and 12), which is too short for
224 the solid particles to settle. After interacting with the flexible barrier, the debris material
225 accumulates behind the barrier and the deposit continues to drain and consolidate. The
226 sampling rate for the impact/overflow stage is set to 1000 Hz and is set to 1 Hz for the
227 consolidation stage.

228 ## 4. Results and interpretation

229 *4.1 Characterization of incoming flow*

230 The basal normal/shear stress and pore fluid pressure for the 4th incoming flow of solid
231 concentration 0.4, 0.5, and 0.6 are shown in Fig. 5. Prior to the 4th release, there is certain
232 amount of deposit above basal sensing module 1, where the pore fluid pressure is lower than
233 the normal stress. As the flow front approach to the module, the basal normal stress and pore

234 fluid pressure quickly rise up. Since the pore fluid pressure equals to normal stress, the flows
235 are fully liquefied, even for flow with solid concentration of 0.6. As the particles lose contact,
236 the measured shear stress is proportional but only 10%-20% of the normal stress. More
237 importantly, this indicates that, during the overflow process, the drag load is not composed of
238 frictional forces. This issue will be further discussed in Section 5.1 Characteristics of total
239 force under overflow.

240 The incoming flow pushes the static deposit behind the barrier to form a hydraulic jump
241 (see Fig. 2b and next section). At the end of overflow process, the flow behind barrier
242 approaches static and a reflected wave is formed to propagate upstream. The reflected wave
243 can be inferred in the rise-up of normal stress and pore pressure. In this stage, the recorded
244 shear stress goes below zero (Fig. 5).

245 *4.2 Overflow kinematics*

246 Substantial overflow is observed in tests 40-4, 50-3, 50-4, and 60-4 (Table 1). The
247 overflow kinematics for surge 4 of solid concentration 0.5 (test 50-4) captured by the
248 downstream video camera 2 (Fig. 3a) can be viewed in Fig. 6 and the Supplementary video.
249 As the flow front approaches the static deposit behind the barrier (Fig. 6a), a hydraulic jump
250 forms, which is characterized with steep jump interface and high downstream flow depth (Fig.
251 6b). Note that flow depth downstream the jump can be derived through the analytical models
252 (based on conservation of mass and momentum, see Chanson 2004). Here we directly
253 measure the upstream and downstream flow depth through ultrasonic and laser sensors (see
254 Fig. 7). Meanwhile, the velocity downstream and upstream the jump can be deduced through
255 the arrival time of the flow front within known distance. The flow of the formed jump

continues to propagate downstream and overflows the barrier (Fig. 6c). The whole overflow process lasts about two seconds and finally returns to static condition (Fig. 6d). The formation of hydraulic jump is not considered in the current design scenario (Fig. 2a) and a schematic diagram of observed overflow kinematics is shown in Fig. 2b.

The observed jump and overflow processes are transient with visible fluctuations in the free surface. This can be further reflected by the measurement of ultrasonic and laser sensors (Fig. 7). As can be seen in Fig. 7b, the measurement of laser sensor (gray line) is characterized with strong fluctuation, thus the moving average (over 0.02 s) is also shown (black line). While the measurement of ultrasonic sensor is smooth, but is much higher than that of the laser sensor, roughly forming an envelope of the laser sensor signal.

The inset in Fig. 7a demonstrates the working principle of the two type of sensors. Both type of sensors emit ultrasonic waves or light waves and receive when the waves reach the surface of flow. The ultrasonic wave is featured with increasing diameter with its travel distance. If the diameter of the ultrasonic wave is larger than the typical wave length of the flow, the wave is reflected back by the crest of flow wave. While the light wave is featured by its strong direction and remains as a point within the measurement range. Thus the light wave could reach the trough and measure details of the flow wave (inset of Fig. 7a). This indicates that the measurement of ultrasonic sensor actually exaggerates the effective flow depth of the unsteady flows (about 20% in Fig. 7b). The reliability of ultrasonic sensor depends on the flow condition and could be low in the filed monitoring of natural geophysical flows. While laser sensor cannot be used for the clean water flow, since the laser wave would transmit through the transparent surface or be reflected elsewhere. The moving average results of laser

278 sensor is adopted in this study for further analysis.

279 *4.3 Cable force and normal impact force*

280 Fig. 8a shows the time history of cable forces under four surge impacts with solid
281 concentration of 0.4. Following the method proposed by Song et al. (2018) which converts the
282 tensile force along cable to the impact force normal to the barrier face, Fig. 8b-e show the
283 detailed characteristics of the normal impact force on the cable during the four surge impacts.
284 Each surge impact is highly transient and followed by a quasi-static consolidation stage. In the
285 first two surge impacts, the lower intermediate cable (blue line) bears the highest impact force
286 (Fig. 8b&c). As overflow imposes drag load to flexible barrier in the last surge, the upper
287 intermediate (black line) cable and top (red line) cable catch up with the lower intermediate
288 one (Fig. 8e). The bottom cable remains the lowest because it is gradually buried by the static
289 debris and no longer subject to the dynamic impact of flowing debris.

290 The experimental results of 0.5 and 0.6 solid concentration series demonstrate similar
291 characteristics (Fig. 9 and 10). Note, there are only three effective impacts in 0.6 solid
292 concentration tests (Fig. 10), since the first surge does not reach the flexible barrier. The key
293 difference between 0.5/0.6 solid concentration impacts and that of 0.4 is that the lower
294 intermediate impact force remains the maximum. This will be further elaborated in term of the
295 degree of liquefaction in Section 5.2 and 5.3. As revealed by Song et al. (2022), prior to
296 reaching the barrier, the incoming flow forms hydraulic jump in the free surface, meanwhile,
297 the flow remixes downward into the static deposit. Thus the overflow not only forms drag
298 load, but also imposes direct impact load due to the momentum exchange to the deep layer. A
299 full description of this overflow process is depicted in Fig. 2b.

5. Characteristics of drag load

5.1 Characteristics of total force under overflow

By assuming the momentum flux of the overflow surges is fully intercepted by the barrier, we compare the theoretical loads with measured loads (Fig. 11a). The theoretical loads are calculated based on the multiple-surge load model (Eqn. 1 and 2). Since the model barrier is simplified without deformation upon impact, α value of 1.5 is adopted, which is recommended for design of rigid barrier by GEO (2020). With the liquefaction of debris material, static pressure coefficient k = 1 is adopted. It is obvious that the surge impacts without overflow can be well predicted by the multiple-surge load model. Unsurprisingly, the surge loads with overflow are excessively overestimated. This is because only part of the momentum flux is effectively resisted by the barrier.

We further predict the total force with consideration of overflow using the overflow load model (Eqn. 3). Since effective stress is not observed in the incoming flow. The frictional term in Eqn. 3 is dropped. The model only considers the turbulence induced drag load (with turbulent coefficient ξ =500 m/s^2; Kwan 2012) and the variation of overflow depth H (by laser sensor 4, Fig. 2b and 7c) for the calculation of static load. With barrier height 0.45 m and flume inclination 12°, the length of active wedge behind the barrier L= 0.45/tan12°=2.12 m. The measured and calculated total force exerted on flexible barrier is compared in Fig. 12. The model predictions (blue line) are generally higher than the measured values (brown line). Nevertheless, these predictions of the overflow load model (Eqn. 3) are substantially lower than those predicted by the multiple-surge load model (Fig. 11a). A direct comparison between the model prediction (Eqn. 3) and measurement is shown in Fig. 11b. The model

322 prediction generally matches well with the physical measurement.

323 Since the first terms in the right hand side of Eqn. 2 and 3 are both characterized with the
324 square of velocity. The ratio of these two terms forms an effective approach to estimate the
325 drag load from the dynamic impact load. Based on the known parameters (h about 0.25 m, L,
326 ξ, α), the drag load ($\frac{\rho v^2}{\xi} gwL$) is about 11% of the dynamic impact load ($\alpha \rho v^2 hw$). In the
327 overflow scenario, under the premise of negligible friction drag, the majority of momentum
328 flux is not resisted by the barrier.

329 Fig. 12 further marks the composition of total force during the overflow of debris flow.
330 In all three cases, the turbulent drag load (Voellmy term in Eqn. 3) is about 2/3 of the
331 maximum static load induced by the increase of overflow depth. This indicates that, the
332 increase in total force (*i.e.*, the general overflow drag force) during the overflow stage is
333 mainly contributed by the static load, rather than the turbulent drag (momentum change).
334 Note this study only covers limited range of solid concentration (flow regime). A thorough
335 experimental investigation on the relative contribution of the static load, turbulent drag, and
336 friction drag (when effective stress exists) is needed.

337 *5.2 Characteristics of load profile*

338 Figure 12 also compares the increase in total force (brown line) and drag load on the top
339 cable (red line). As revealed above, the static load substantially contributes to the total force.
340 Even so, the increase of drag load in the top cable is still lower than that of the turbulent drag
341 (Voellmy term in Eqn. 3), denoting part of the drag load is redistributed downwards. Thus we
342 further plot the cable load profile at the moment of peak total force to elucidate the
343 distribution of the drag load behind barrier. In Fig. 13, the abscissa represents the normal

force and the ordinate represents the height of flexible barrier. The four cables are located at 0.00, 0.15, 0.30, and 0.45 m, respectively. For overflow with 0.5 and 0.6 solid concentration, the measured results show that the maximum load stays on the lower intermediate cable. This finding is consistent with that of Song et al. (2022), where only direct normal impact is studied. This means that, in the overflow stage, the momentum exchange does not merely occur around the top cable. Rather, the deposits of the previous surges are remixed and the momentum is exchanged to the deep layer to form impact load. A schematic diagram of the remixing process induced by the overflow is depicted in Fig. 2b.

The bearing capacity of anchors is the key parameter for debris-flow flexible barrier design. The current multiple-surge impact and overflow load models do not consider the downward momentum transfer. Thus the model prediction may not be conservative for engineering design. To enhance the robustness of the whole flexible barrier system, the bearing capacity of the lower intermediate cable should be further improved.

The load profile of 0.4 solid concentration is different, with the peak cable load on the upper intermediate cable (Fig. 13). We adopt the measurement of basal sensing module 2 right behind the barrier (Fig. 3a) to explain this discrepancy.

5.3 Basal stresses and pore fluid pressure

To further explain the discrepancy in load profile (Fig. 13), the state of debris-flow deposits behind the barrier are analyzed through the measured normal/shear stresses and pore fluid pressure. For simplicity, only the responses of the 4th overflow surges are shown. For tests 50-4 and 60-4, the pore fluid pressure closely follows the variation of normal stress (Fig. 14 b&c), denoting full liquefaction due to the remixing of the 4th surge. As a result of the low

366 effective grain contact, the measured shear stress is negligible, although the deposit is lying
367 on a 12° slope. However, the sign of measured shear stress is indicative to the mixing
368 direction behind the barrier. The shear stress rises with the increasing normal stress, denoting
369 the downstream flow direction along the flume base. As the normal stress peaks, the shear
370 stress shifts from positive to negative, denoting the upstream movement along the flume base.
371 Due to the opaque feature of debris-flow slurry, further insights into the overflow-induced
372 remixing is rather difficult. Some transparent two-phase flow material, in combination with
373 the PIV technology, has the potential to further reveal this critical process (Sanvitale and
374 Bowman 2012).

375 As with the cable load profile (Fig. 13a), the response of test 40-4 demonstrates quite
376 different pattern (Fig. 14a). The magnitude of basal pore fluid pressure is much lower than
377 that of the normal stress and this difference denotes the nontrivial effective stress. Before the
378 arrival of surge 4, the deposit of antecedent three surges is partially drained. More importantly,
379 the 4th surge fails to fully remix and liquefy the drained deposit. The measured shear stress
380 during overflow is also nontrivial. This helps to explain the discrepancy in the load profile in
381 Fig. 13. As the deposit cannot be fully remixed, the drained deposit with effective stress
382 inhibits the downward momentum transfer to the base of flume, and thus the peak cable load
383 concentrates on the upper intermediate cable. Based on the distinct responses in the 0.4 and
384 0.5/0.6 solid concentration overflow, we conclude that the re-liquefaction is a prerequisite for
385 the downward momentum transfer.

6. Discussion on the overflow load model

6.1 Source of error in the model prediction

Comparison between the experimental measurement and overflow load model prediction demonstrates some discrepancy (Fig. 12). The possible source of error in term of flow depth H, velocity v, and turbulent coefficient ξ in Eqn. 3 is discussed in this section.

The formation of hydraulic jump is accompanied with strong fluctuations in the free surface (Fig. 6b&c). We adopt the measurement of laser senor, which could largely exclude the spurious signal in ultrasonic sensors induced by the uneven flow surface. Due to the influence of the sidewall, these fluctuations are deflected into the midstream of flume, where the flow depth H is measured. Thus the flow depth is to some extent magnified by the localized fluctuation. Moreover, in the transient overflow scenario, the flow trajectory is deflected upwards by the barrier, which makes the measured flow depth higher than that in the steady overflow condition. Thus the calculated static load is higher than the true value.

The frontal velocity v is adopted for calculation, without correction of the velocity profile (Faug et al. 2012) along flow depth. More importantly, the downward momentum transfer renders the velocity profile even complex. This could be another main source of error.

The turbulent coefficient ξ is used to macroscopically reflect the degree of turbulence (Voellmy 1955), ranging from 100 to several thousand (Schneider et al. 2010). Under the circumstance of no effective stress, the turbulent drag is the only source of drag load. Sensitive analysis is not a focus of this study. However, it is clear that by adopting different turbulent coefficients for the cases with varying solid concentration, the model prediction could well match the measurement. Indeed, from the captured overflow kinematics (Fig. 6

and Supplementary video), the flow with solid concentration 0.4 is the most turbulent; while flow with solid concentration 0.6 is coherent without obvious fluctuation. This indicates that it is not feasible to use one set of parameters to match debris flows with distinct characteristics (*i.e.*, solid concentration).

6.2 Assessment of existing overflow load model

The increase of load exerted on flexible barrier is composed of the turbulent drag load of overflow and static load due to the increase in flow depth. Somehow in the three cases with solid concentration 0.4, 0.5, and 0.6, the static load dominates over the drag load (Fig. 12). More importantly, the drag load is not merely the drag force around the interface between the flowing layer and the deposited debris (see Fig. 2a). The overflow fully remixes the deposit of solid concentration 0.5 and 0.6 (Fig. 14b&c), denoting that part of the momentum has been transferred downward to directly impact on the barrier (Fig. 13). While for the case of solid concentration 0.4, due to the high permeability at low solid concentration (Iverson and George 2014), the deposit quickly drains to attain effective stress and the deposit is only partially remixed (Fig. 14a). As a result, the maximum cable load shifts upwards to the upper intermediate cable (Fig. 13).

Despite the overall consistence between model prediction and experimental measurement, the revealed physical process is different from the assumption in existing overflow load model (Fig. 2a). Specifically, the pressure distribution behind the barrier is not hydrostatic and the downward momentum transfer makes the velocity profile rather complicated (Fig. 2b). With the model assumption in Fig. 2a, the designed cable load of flexible barrier might be underestimated. This experimental study also reveals the complexity

of debris-barrier interaction, where the properties of debris flow itself (*i.e.*, solid-fluid interaction and evolution of effective stress) could have primary influence.

It should be noted that, this study evaluates the existing overflow load model based on the measured flow depth and velocity downstream the hydraulic jump (i.e., h_3 and v_3 in Fig. 2b). Whereas in practical engineering design, the only known information is the incoming flow depth and velocity (h_1 and v_1 in Fig. 2b). A rigorous overflow load model for dry granular flow has been proposed by Faug et al. (2012), which strictly follows the conservation of momentum through the inflow and outflow information. More importantly, the model only uses incoming flow depth and velocity to predict the outflow information and thus the total force on barrier. A similar overflow load model is warranted for two-phase debris flows, although the debris-barrier interaction is much complicated with hydraulic jump and remixing of deposits. By taking the zone affected by the barrier as control volume (see Fig. 2b), we can largely bypass the complex interaction around the barrier. The controlled physical experiments with visualization of flow field and development of new overflow load model are under progress.

7. Conclusions

The estimation of load by debris-flow overflow is not only a key procedure for design of multiple debris-resisting barriers, but also serves as a stringent approach to inspect the dynamics of this two-phase geophysical flow. Through experimentally investigating the overflow kinematics, total impact load, load profile, and state of deposit behind the barrier, the key processes of debris flow overflowing flexible barrier is revealed. The possible source of error in the prediction of overflow load model and the limitation of current model are also

452 discussed. The key conclusions of this study may be drawn as follows:

453 1. The performance of ultrasonic sensor and laser sensor for measuring unsteady flow depth
454 is compared. Due to the distinct working principles, ultrasonic sensor could only detect
455 the crest or splash of flow waves as the free surface, regardless of the solid concentration
456 of the flows. Thus the flow depth under turbulent flow condition could be substantially
457 overestimated in the field monitoring. While laser sensor could characterize many details
458 (fluctuations) of the turbulent flow, but can only be used for the opaque flow surface (at
459 high solid concentration).
460 2. Hydraulic jump forms as the incoming flow approaches the static deposit behind the
461 barrier, which substantially elevates the overflow depth at the flexible barrier. This
462 process is a result of the complicated debris-barrier interaction and is not considered in
463 the current overflow load model.
464 3. The basal measurement confirms negligible effective stress for solid concentration up to
465 0.6. Thus the turbulent drag seems to be the only component of the drag load. Ratio
466 between the turbulent drag and dynamic impact indicates that about 10% of the
467 momentum flux is resisted in the overflow process. This is an effective approach to
468 estimate the drag load in the scenario of negligible effective stress. Decomposition of the
469 total force further reveals that the increase in total force is actually dominated by the static
470 load due to elevated flow depth, rather than the turbulent drag (momentum change).
471 4. The re-liquefaction is a prerequisite for the downward momentum transfer. For the 0.4
472 solid concentration flow, the deposit is partially drained and the effective stress hinders
473 the remixing of static debris to the flume base. As a result, the maximum cable load

concentrates on the upper intermediate cable. In contrast, the deposits for high (0.5 and 0.6) solid concentration overflow cases remain liquefied for the four impact-overflow surges, and the position of maximum cable load shifts downwards.

This experimental study reveals the physical processes (hydraulic jump and overflow) and load characteristics of debris flow overtopping a model barrier, which is fundamental and crucial for understanding the debris-flow overflow mechanisms. Nevertheless, the flow depth and velocity are directly measured downstream the hydraulic jump as inputs for the overflow model evaluation. Thus it is far from enough for practical engineering design where only the incoming-flow information is available. A model considering the full physical processes and replying on the incoming-flow information is warranted.

Conflicts of Interests:

The authors declare no conflicts of interests.

Acknowledgement

The authors acknowledge the financial support from the National Natural Science Foundation of China (grant No. 42077256 and 41925030), the CAS "Light of West China" Program, and the Sichuan Science and Technology Program (grant No. 2020YJ0002). Technical support from the DDFORS (Dongchuan Debris Flow Observation and Research Station) of Chinese Academy of Sciences is also acknowledged.

References

Berger C, Denk M, Graf C, Stieglitz L, Wendeler C, 2021, Practical guide for debris flow and hillslope debris flow protection nets. WSL Berichte 113. 79 p.

Chanson H (2004) Hydraulics of open channel flow. Elsevier.

Chen Z, He S, Shen W, Wang D (2021a) Effects of defense-structure system for bridge piers on two-phase debris flow wakes. Acta Geotechnica 1-21.

Chen Z, Rickenmann D, Zhang Y, He S (2021b) Effects of obstacle's curvature on shock

499 dynamics of gravity-driven granular flows impacting a circular cylinder. Engineering
500 Geology 293: 106343.

501 Cui P, Chen X, Wang Y, Hu K, Li, Y (2005) Jiangjia Ravine debris flows in south-western
502 China. In Debris-flow hazards and related phenomena (pp.565-594). Springer, Berlin,
503 Heidelberg.

504 Faug T, Beguin R, Chanut B (2009) Mean steady granular force on a wall overflowed by
505 free-surface gravity-driven dense flows. Physical Review E 80(2): 021305.

506 Faug T, Caccamo P, Chanut B (2012) A scaling law for impact force of a granular avalanche
507 flowing past a wall. Geophysical research letters 39(23).

508 Fei XJ, Kang ZC, Wang YY, (1991) Effect of Fine Grain and Debris Flow Slurry Bodies on
509 Debris Flow Motion. Mountain Research 9(3): 143-152 (in Chinese).

510 GEO (2020) Enhanced Technical Guidance on Design of Rigid Debris-resisting Barriers.
511 Technical Guidance Note No. 52 (TGN 52). Geotechnical Engineering Office, Civil
512 Engineering Department of CEDD, HKSAR.

513 Hübl J, Suda J, Proske D, Kaitna R, Scheidl C (2009) Debris flow impact estimation. In
514 *Proceedings of the 11th international symposium on water management and hydraulic*
515 *engineering*, Ohrid, Macedonia.

516 Iverson RM, Ouyang C (2015) Entrainment of bed material by Earth‐surface mass flows:
517 Review and reformulation of depth‐integrated theory. Reviews of Geophysics 53(1):
518 27-58.

519 Iverson RM, Reid ME, Logan M, LaHusen RG, Godt JW, Griswold JP (2011) Positive
520 feedback and momentum growth during debris-flow entrainment of wet bed sediment.
521 Nature Geoscience 4(2): 116-121.

522 Iverson RM, George DL (2014) A depth-averaged debris-flow model that includes the effects
523 of evolving dilatancy. I. Physical basis. In *Proceedings of the Royal Society of London A:*
524 *Mathematical, Physical and Engineering Sciences* 470(2170): 20130819.

525 Kaitna R, Palucis MC, Yohannes B, Hill KM, Dietrich WE (2016) Effects of coarse grain size
526 distribution and fine particle content on pore fluid pressure and shear behavior in
527 experimental debris flows. Journal of Geophysical Research: Earth Surface 121(2):
528 415-441.

529 Kwan JSH (2012) Supplementary technical guidance on design of rigid debris-resisting
530 barriers. GEO Report No. 270. Geotechnical Engineering Office, HKSAR Government

531 Kwan JSH, Koo RCH, Ng CWW (2015) Landslide mobility analysis for design of multiple

532 debris-resisting barriers. Canadian Geotechnical Journal 52(9): 1345-1359.

533 Kong Y, Li X, Zhao J (2021) Quantifying the transition of impact mechanisms of geophysical
534 flows against flexible barrier. Engineering Geology 106188.

535 Liu W, He S, Chen Z, Yan S, Deng Y (2021) Effect of viscosity changes on the motion of
536 debris flow by considering entrainment. Journal of Hydraulic Research 59(1): 120-135.

537 McArdell BW, Bartelt P, Kowalski J (2007) Field observations of basal forces and fluid pore
538 pressure in a debris flow. Geophysical research letters 34(7).

539 Ng CWW, Choi CE, Majeed U, Poudyal S, De Silva WARK (2019) Fundamental framework
540 to design multiple rigid barriers for resisting debris flows. In Proceedings of the 16th
541 Asian regional conference on soil mechanics and geotechnical engineering. 14th to 18th
542 October.

543 Ng CWW, Majeed U, Choi CE, De Silva WARK (2021) New impact equation using barrier
544 Froude number for the design of dual rigid barriers against debris flows. Landslides
545 1-13.

546 Ouyang C, He S, Tang C (2015) Numerical analysis of dynamics of debris flow over erodible
547 beds in Wenchuan earthquake-induced area. Engineering Geology 194: 62-72.

548 Sanvitale N, Bowman ET (2012) Internal imaging of saturated granular free-surface flows.
549 International Journal of Physical Modelling in Geotechnics 12(4): 129-142.

550 Scheidl C, Chiari M, Kaitna R, Müllegger M, Krawtschuk A, Zimmermann T, Proske,D (2013)
551 Analysing debris-flow impact models, based on a small scale modelling approach.
552 Surveys in Geophysics 34(1): 121-140.

553 Schneider D, Bartelt P, Caplan‐Auerbach J, Christen M, Huggel C, McArdell BW (2010)
554 Insights into rock‐ice avalanche dynamics by combined analysis of seismic recordings
555 and a numerical avalanche model. Journal of Geophysical Research: Earth Surface
556 115(F4).

557 Speerli J, Hersperger R, Wendeler C, Roth A (2010) Physical modeling of debris flows over
558 flexible ring net barriers. In Physical Modelling in Geotechnics (pp. 1309-1314). CRC
559 Press.

560 Song D, Zhou GGD, Choi CE, Zheng Y (2019a) Debris flow impact on flexible barrier:
561 effects of debris-barrier stiffness and flow aspect ratio. Journal of Mountain Science
562 16(7): 1629-1645.

563 Song D, Zhou GGD, Xu M, Choi CE, Li S, Zheng Y (2019b) Quantitative analysis of
564 debris-flow flexible barrier capacity from momentum and energy perspectives.

565 Engineering Geology 251: 81-92.

566 Song D, Bai Y, Chen X, Zhou GGD, Choi CE, Pasuto A, Peng P. (2022) Assessment of debris
567 flow multiple-surge load model based on the physical process of debris-barrier
568 interaction. Landslides. DOI:10.1007/s10346-021-01778-3

569 Song D, Chen X, Zhou GGD, Lu X, Cheng G, Chen Q. (2021) Impact dynamics of debris
570 flow against rigid obstacle in laboratory experiments. Engineering Geology 106211.

571 Tan DY, Yin JH, Qin JQ, Zhu ZH, Feng WQ (2020) Experimental study on impact and
572 deposition behaviours of multiple surges of channelized debris flow on a flexible barrier.
573 Landslides 17(7): 1577-1589.

574 Vicari H, Ng C.W.W., Nordal S, Thakur V, De Silva WARK., Liu H, and Choi CE. (2021) The
575 Effects of Upstream Flexible Barrier on the Debris Flow Entrainment and Impact
576 Dynamics on a Terminal Barrier. Canadian Geotechnical Journal.
577 https://doi.org/10.1139/cgj-2021-0119

578 Voellmy A (1955) Uber die Zerstorungskraft von Lawinen. Schweiz. Bauztg 73 (12): 159–
579 162.

580 Wang Y, Liu X, Yao C, Li Y, Liu S, Zhang X (2018) Finite release of debris flows around
581 round and square piers. Journal of Hydraulic Engineering 144(12): 06018015.

582 Wendeler C (2016). Debris flow protection systems for mountain torrents - basic principles
583 for planning and calculation of flexible barriers. WSL Berichte 44. [ISSN 2296-3456.]

584 Wendeler C, Volkwein A, Roth A, Herzog B, Hahlen N, Wenger M (2008) Hazard prevention
585 using flexible multi-level debris flow barrier. In 11th Interpraevent Congress (pp.
586 547-554).

587 Wendeler C, Volkwein A, McArdell BW, Bartelt P (2019) Load model for designing flexible
588 steel barriers for debris flow mitigation. Canadian Geotechnical Journal 56(6): 893-910.

589 Wendeler C, Volkwein A, Denk M, Roth A, Wartmann S (2007) Field Measurements Used for
590 Numerical Modelling of Flexible Debris Flow Barriers, In: CL Chen, JJ Major (eds).
591 Proceedings of Fourth International Conference on Debris Flow Hazards Mitigation:
592 Mechanics, Prediction, and Assessment, Chengdu, China, 10–13 September 2007. pp.
593 681–687.

594 Wong LA, Lam HWK (2018b) Spillage Mechanism of Landslide Debris Intercepted by Rigid
595 Barriers and Deflectors to Prevent Spillage (GEO Technical Note No. 5/2018).
596 Geotechnical Engineering Office, Hong Kong

597 Yang HJ, Hu KH, Wei FQ (2013) Methods for computing rheological parameters of

598 debris-flow slurry and their extensibilities. Shuili Xuebao 44(11): 1338-1346. (in
599 Chinese)

600 Zhang B, Huang Y (2021) Unsteady overflow behavior of polydisperse granular flows against
601 closed type barrier. Engineering Geology 280: 105959.

602 Zhang S, Liu Y, Bate B, Peng DL, Li C, Zhan LT (2021) Quantitative human risk analysis of
603 2015 Shenzhen dump failure considering influence of urbanization. Journal of Mountain
604 Science 18(6): 1439-1457.

List of figures

Fig. 1. Closely installed multiple debris-flow flexible barriers upstream a railway at west of Beijing.

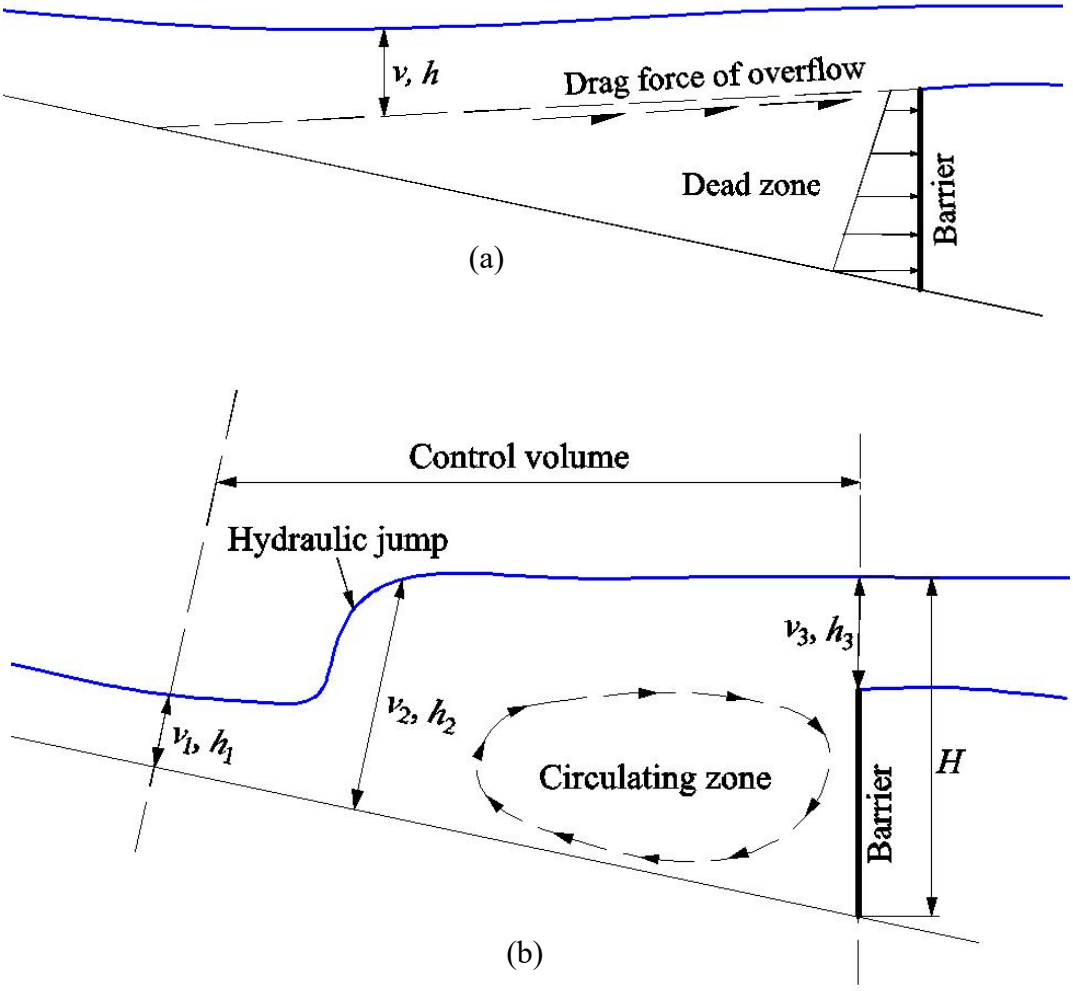

Fig. 2. Debris flow overflowing the barrier (a) overflow with dead zone forming behind the barrier (Kwan 2012; Wendeler *et al*. 2019); (b) overflow with hydraulic jump and circulating zone behind the barrier. Load from discrete boulders is not considered. v_1 and h_1: incoming flow velocity and depth; v_2 and h_2: flow velocity and depth after hydraulic jump; v_3 and h_3: flow velocity and depth over the barrier.

(a)

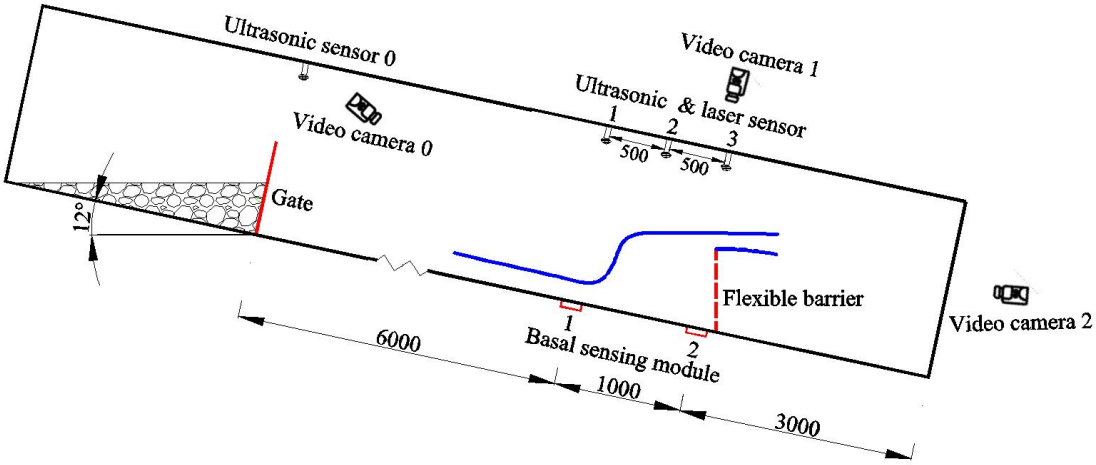

(b)

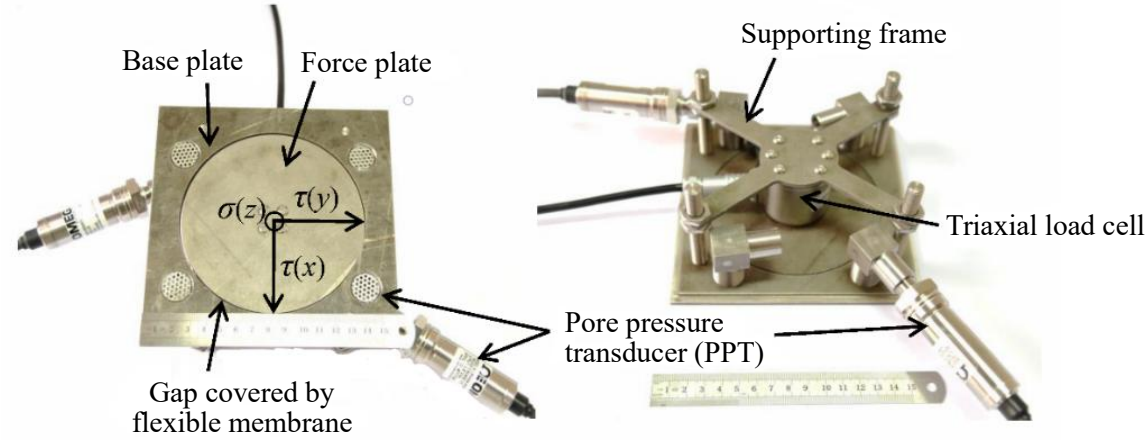

(c)

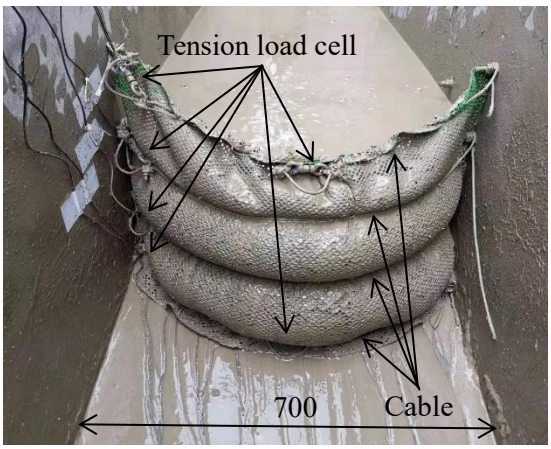

Fig. 3. Model setup and instrumentation (a) flume setup, the model flexible barrier is installed 150 mm behind basal sensing module 2; (b) up side and bottom side of basal sensing module; (c) model flexible barrier setup. All units in mm.

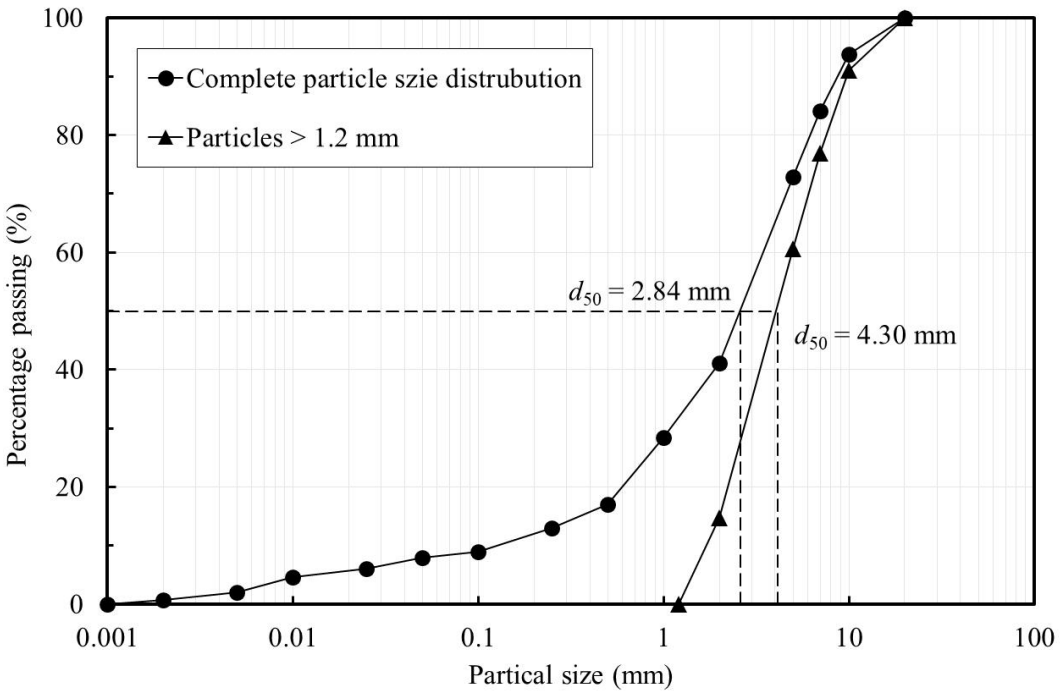

Fig. 4. Particle size distribution of debris flow material.

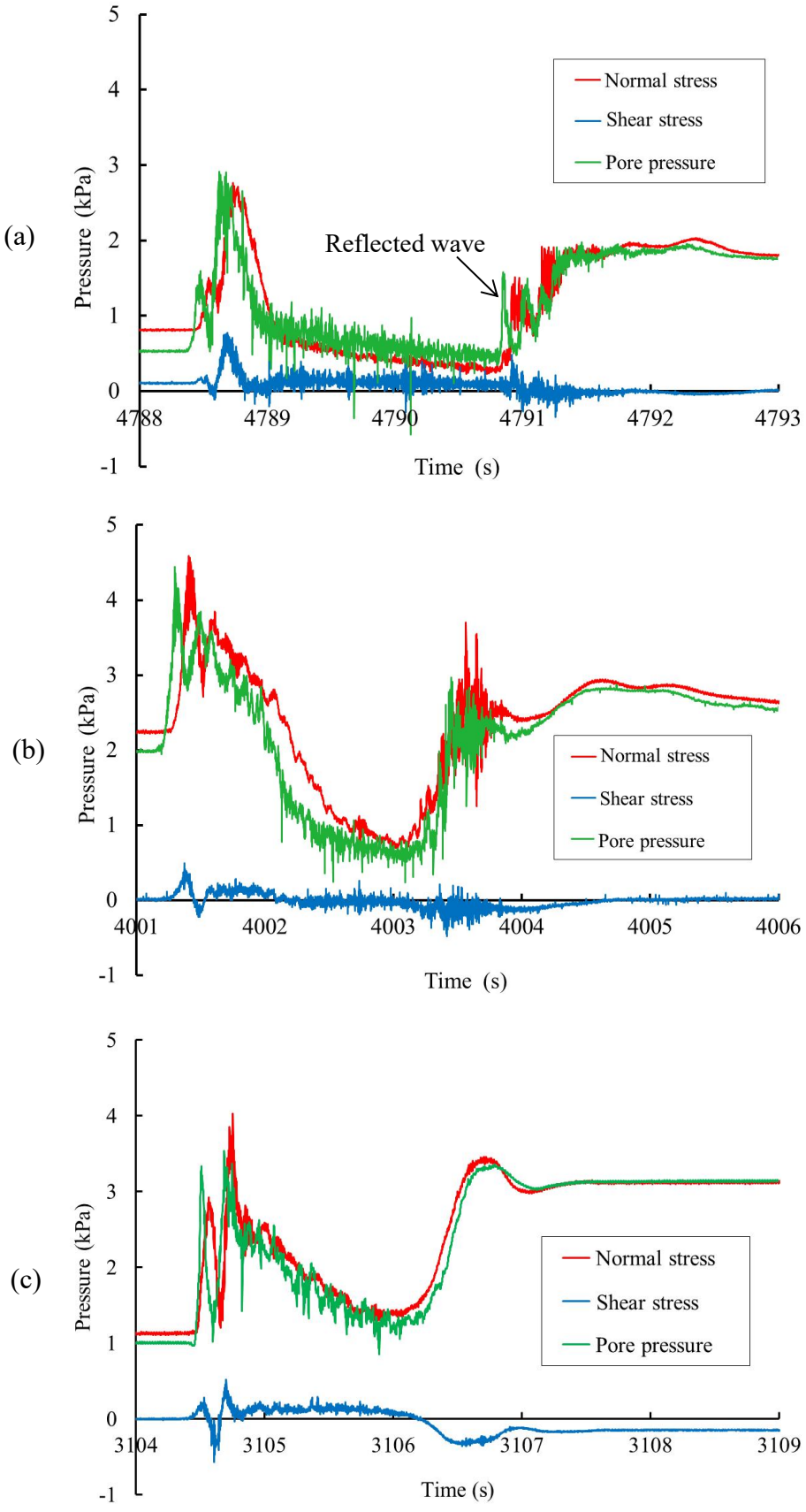

Fig. 5. Characterization of flow regime at basal sensing module 1 for test (a) 40-4; (b) 50-4; and (c) 60-4.

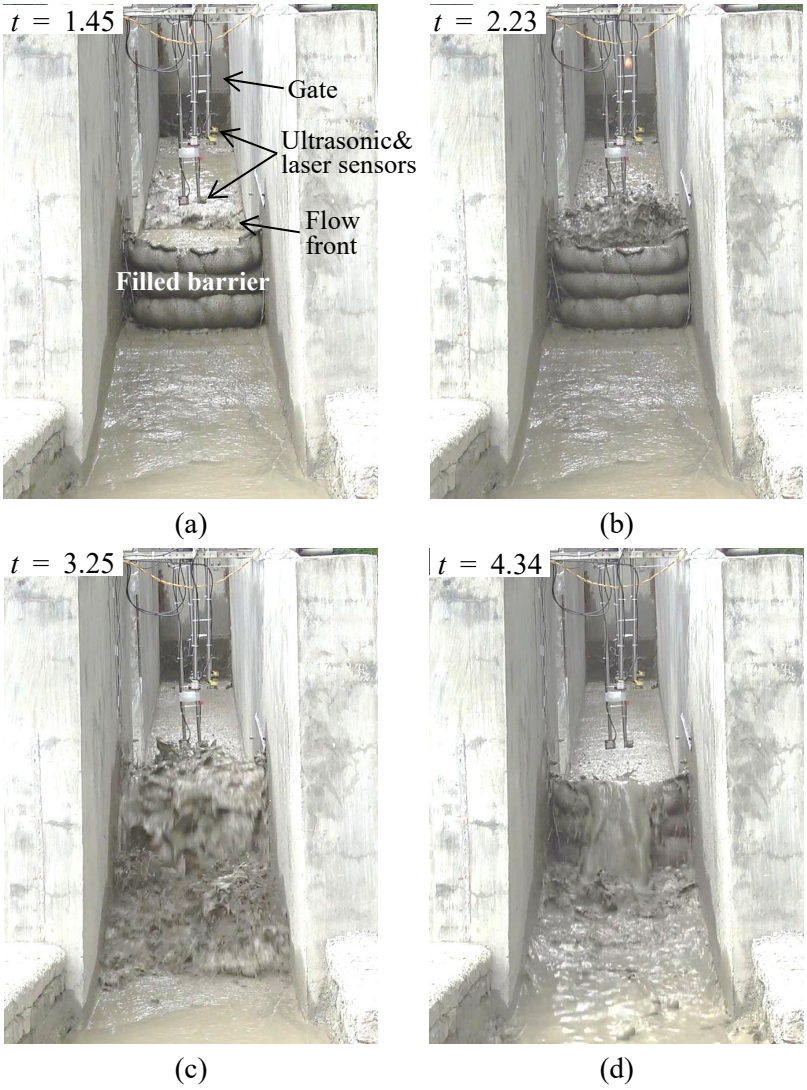

Fig. 6. Processes of surge 4 of solid concentration 0.5 (test 50-4) overflowing the barrier (a) t = 1.45 s, incoming flow; (b) t = 2.23 s, formation of hydraulic jump; (c) t = 3.25 s, overflow; and (d) t = 4.34 s, end of overflow. t = 0 s denotes opening of the gate.

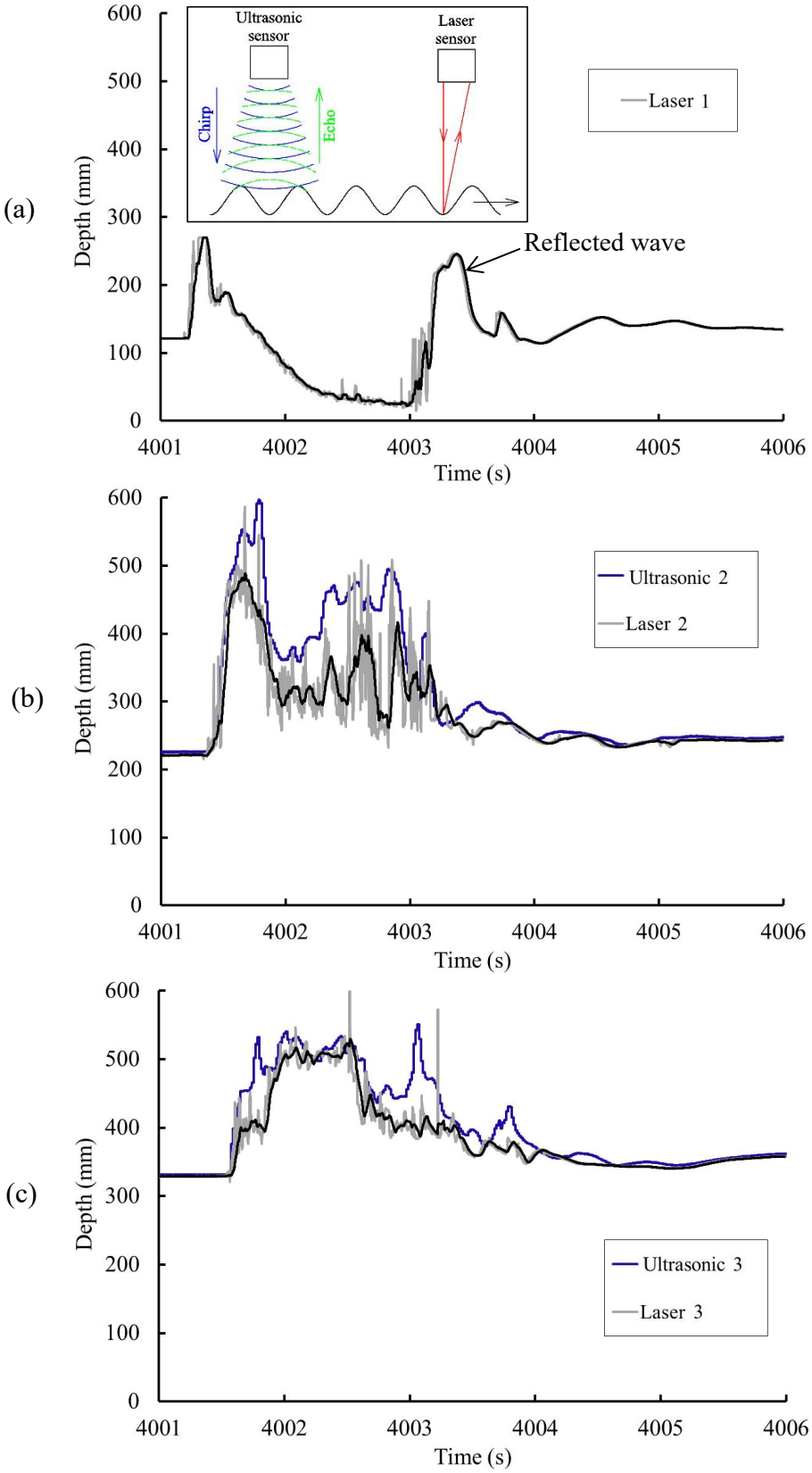

Fig. 7. Measured flow depth of surge 4 of solid concentration 0.5 (test 50-4) at (a) laser sensor 1 (ultrasonic 1 malfunctioned), inset: working principle of ultrasonic sensor and laser sensor on undulating surface; (b) ultrasonic and laser sensor 2; and (c) ultrasonic and laser sensor 3.

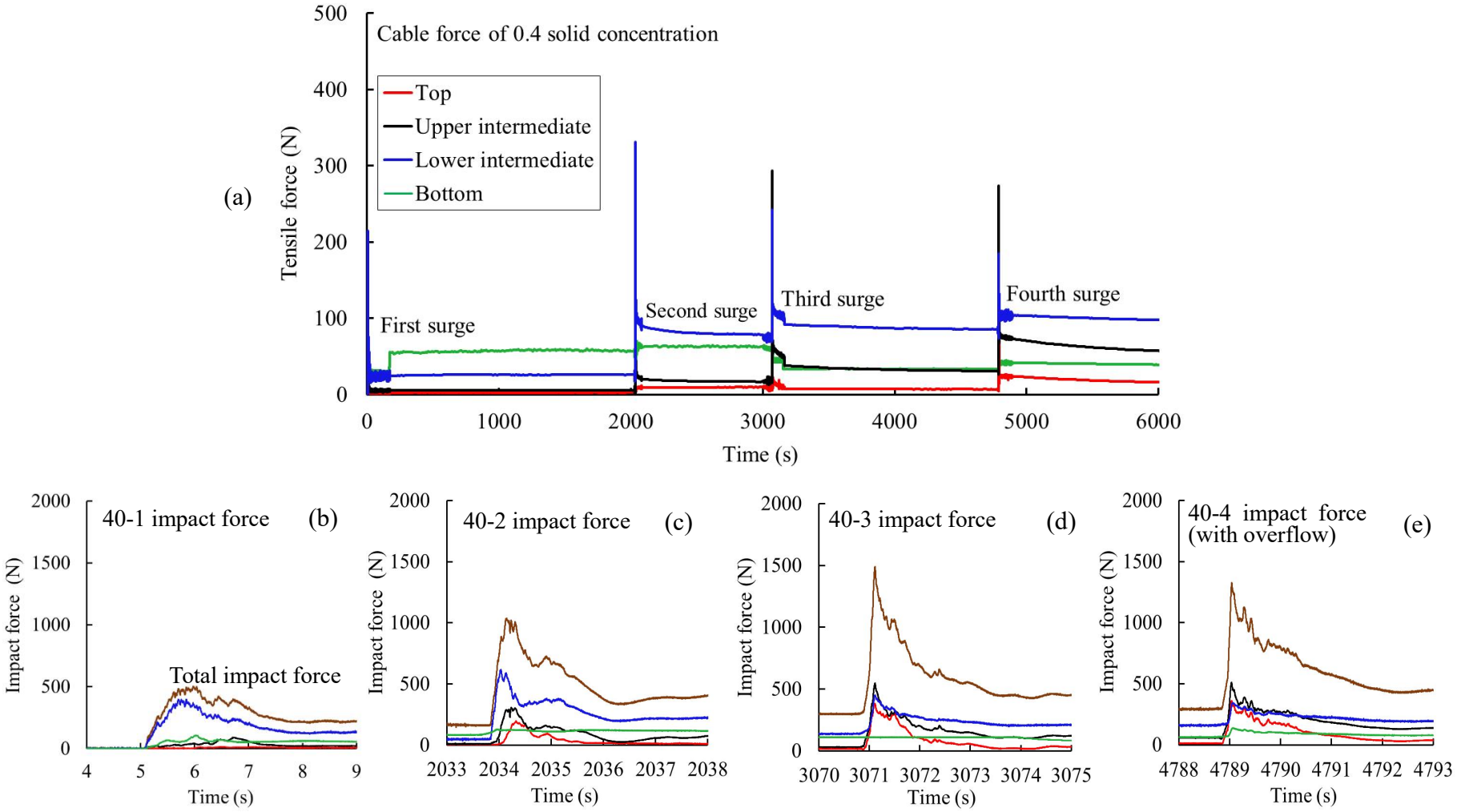

Fig. 8. Measured cable force and calculated normal impact force of 0.4 solid concentration impact (a) cable force; (b-e) normal impact force of test 40-1, 40-2, 40-3, and 40-4. The total normal impact force (summation of normal impact forces on four cables) is also shown.

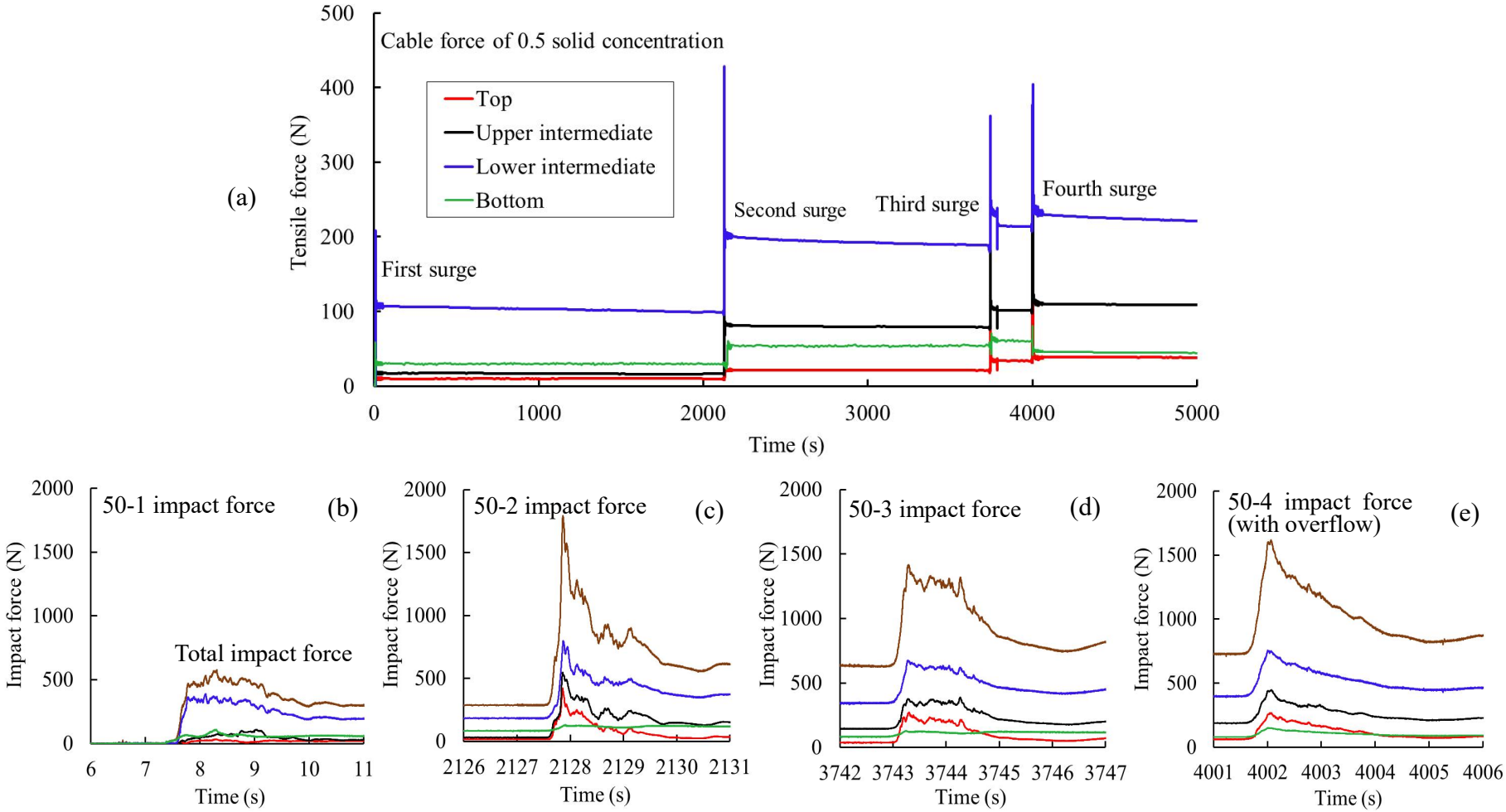

Fig. 9. Measured cable force and calculated normal impact force of 0.5 solid concentration impact (a) cable force; (b-e) normal impact force of test 50-1, 50-2, 50-3, and 50-4.

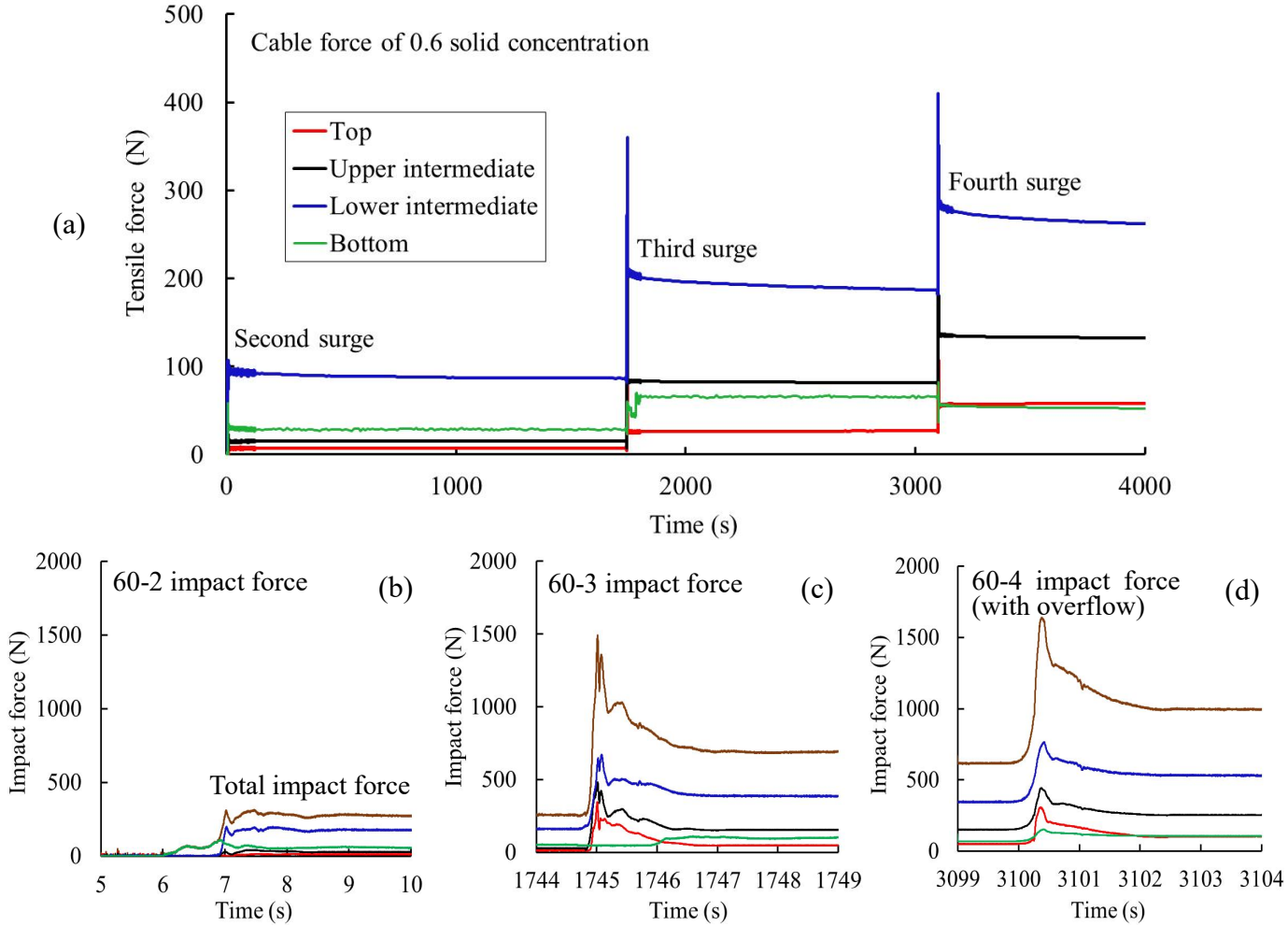

Fig. 10. Measured cable force and calculated normal impact force of 0.6 solid concentration impact (a) cable force; (b-d) normal impact force of test 60-2, 60-3, and 60-4.

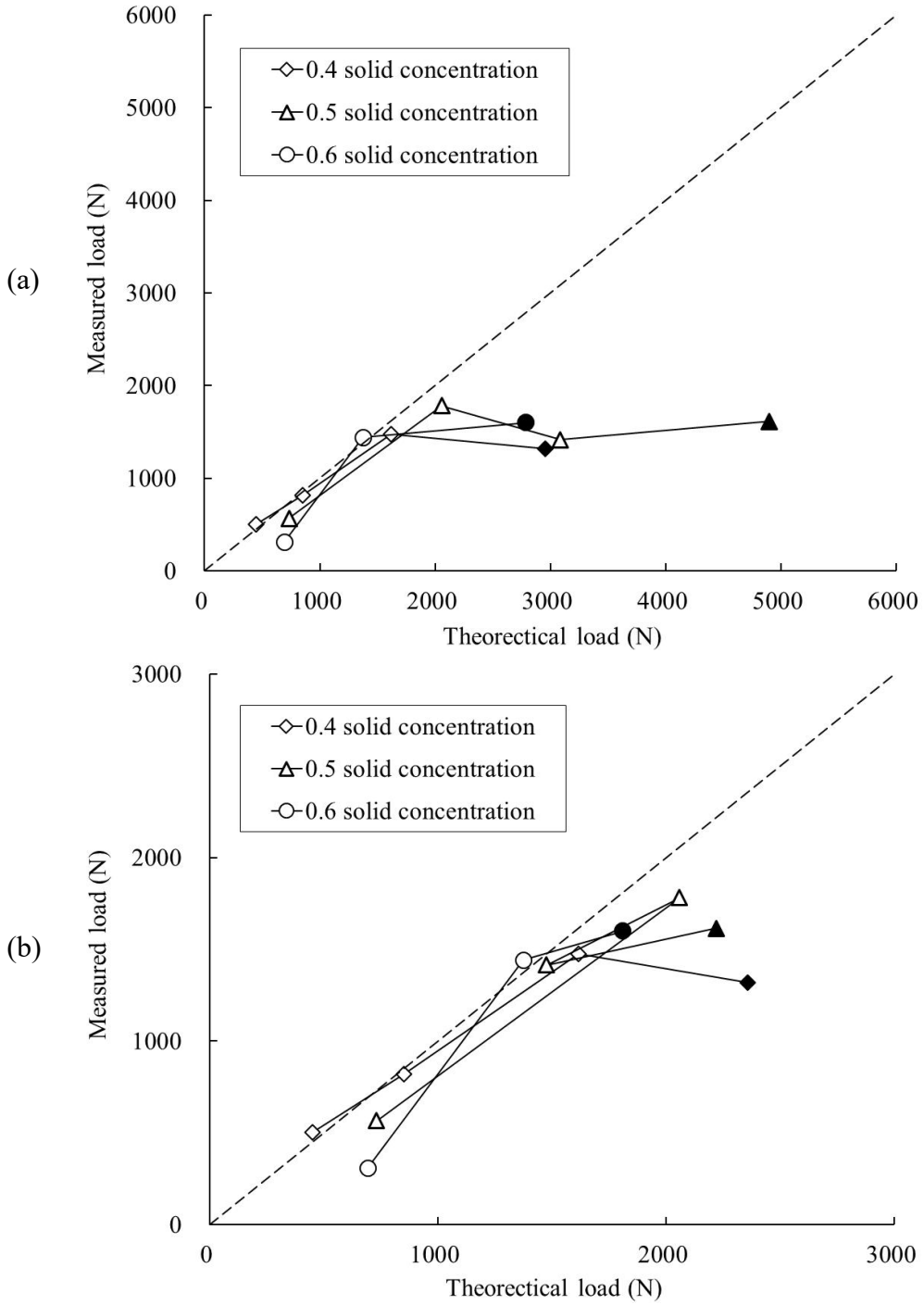

Fig. 11. Comparison between theoretical load (with dynamic pressure coefficient α=1.5 and static pressure coefficient k=1) and measured load (a) assuming the momentum of overflowing surge is completely resisted by the barrier; (b) with consideration of overflow. Solid symbols denote results of the 4th (overflow) surges.

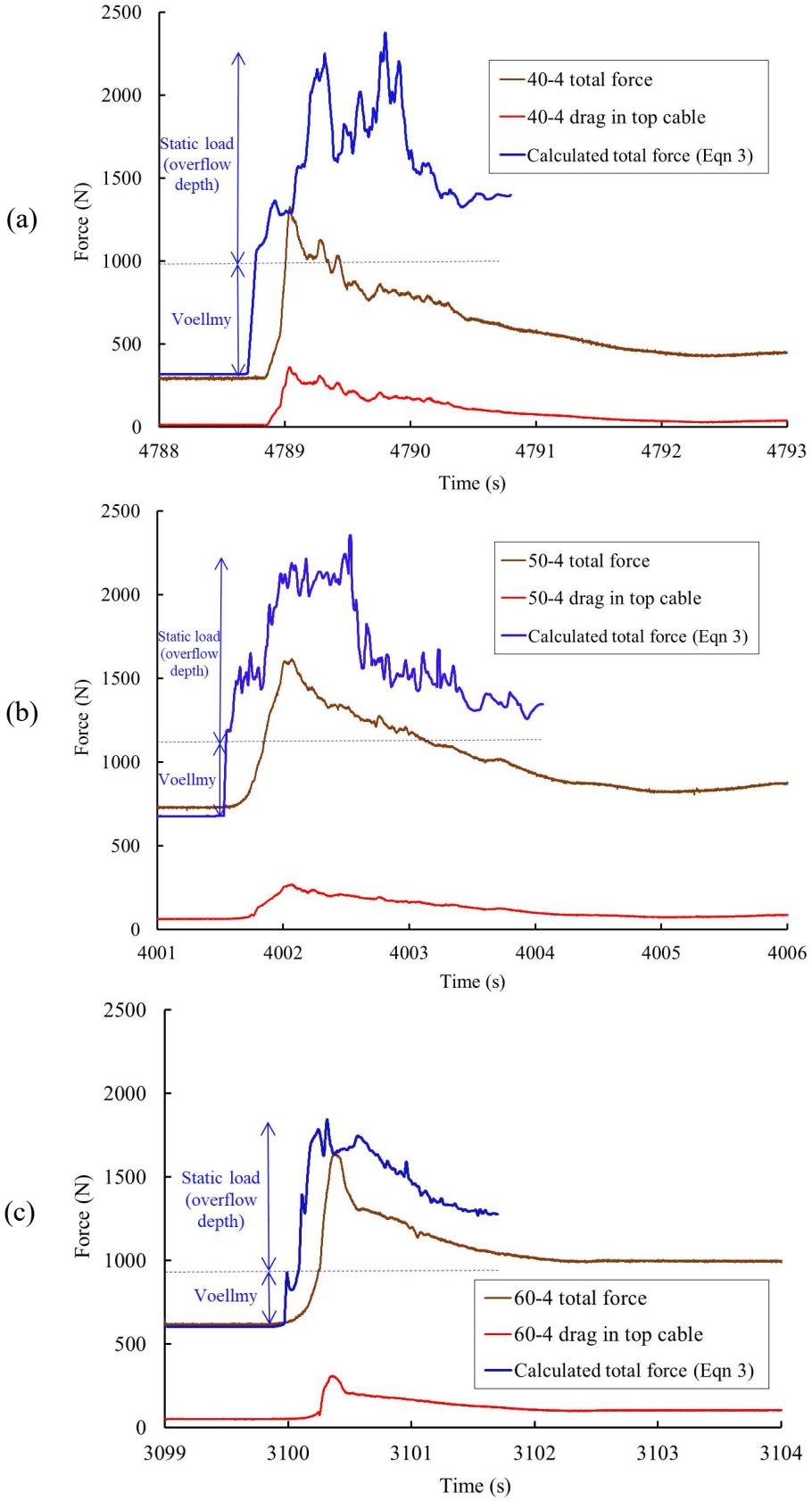

Fig. 12. Comparison between measured and calculated total force for test (a) 40-4; (b) 50-4; and (c) 60-4.

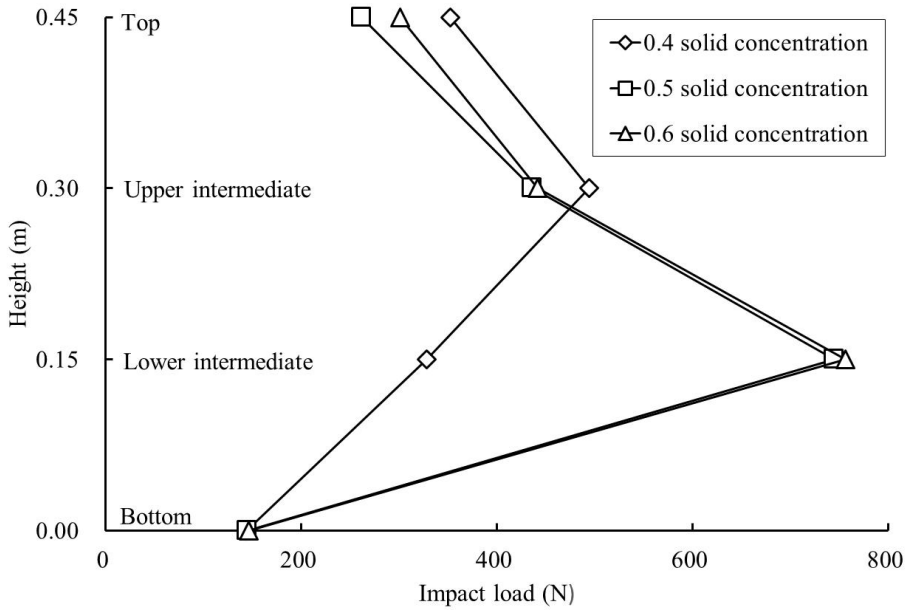

Fig. 13. Cable load profile of normal impact force at the moment of peak drag force

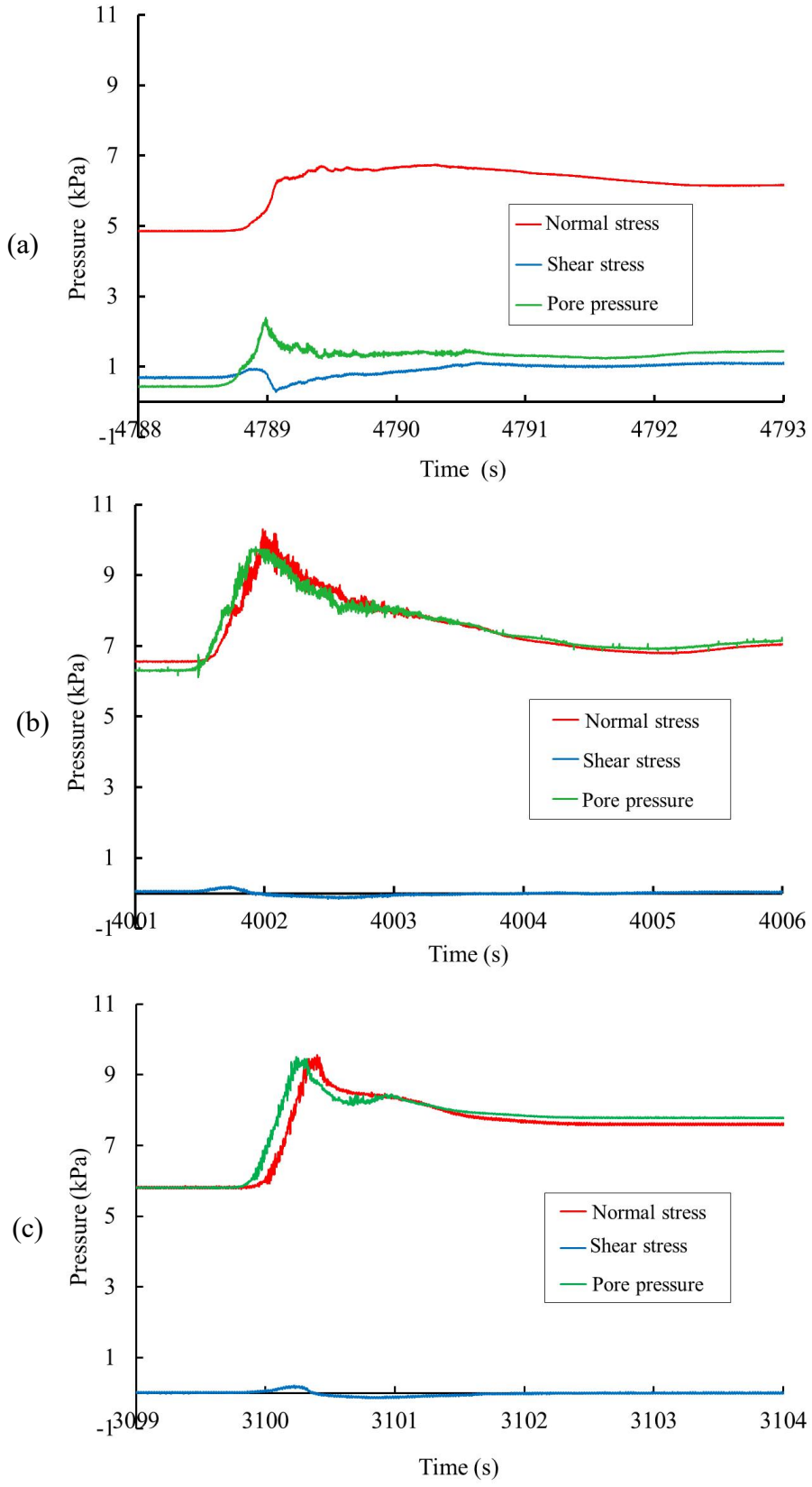

Fig. 14. Evolution of normal/shear stress and pore fluid pressure at basal sensing module 2 of test (a) 40-4; (b) 50-4; and (c) 60-4.